

Flexural Ridges, Trenches, and Outer Rises Around Coronae on Venus

DAVID T. SANDWELL

Geological Research Division, Scripps Institution of Oceanography, La Jolla, California

GERALD SCHUBERT

Department of Earth and Space Sciences, Institute of Geophysics and Planetary Physics, University of California, Los Angeles

High-resolution altimetry collected by the Magellan spacecraft reveals trench and outer rise topographic signatures around major coronae (e.g. Eithinoha, Heng-O, Artemis, and Latona). In addition, Magellan synthetic aperture radar images show circumferential fractures in areas where the plates are curved downward. Both observations suggest that the lithosphere around coronae is flexed downward by the weight of the overriding coronal rim or by the negative buoyancy of subducted lithosphere. We have modelled the trench and outer rise topography as a thin elastic plate subjected to a line load and bending moment beneath the corona rim. The approach was tested at northern Freyja Montes where the best fit elastic thickness is 18 km, in agreement with previously published results. The elastic thicknesses determined by modelling numerous profiles at Eithinoha, Heng-O, Artemis, and Latona are 15, 40, 37, and 35 km, respectively. At Eithinoha, Artemis, and Latona where the plates appear to be yielding, the maximum bending moments and elastic thicknesses are similar to those found at the Middle America, Mariana, and Aleutian trenches on Earth, respectively. Estimates of effective elastic thickness and plate curvature are used with a yield strength envelope model of the lithosphere to estimate lithospheric temperature gradients. At Heng-O, Artemis, and Latona, temperature gradients are less than 10 K/km, which correspond to conductive heat losses of less than one half the expected average planetary value. We propose two scenarios for the creation of the ridge, trench, and outer rise topography: differential thermal subsidence and lithospheric subduction. The topography of Heng-O is well matched by the differential thermal subsidence model. However, at Artemis and Latona the amplitudes of the trench and outer rise signatures are a factor of 5 too large to be explained by thermal subsidence alone. In these cases we favor the lithospheric subduction model wherein the lithosphere outboard of the corona perimeter subducts (rolls back) and the corona diameter increases.

INTRODUCTION

The lithospheres of Earth and Mars are known to have elastic upper layers that undergo flexural deformation [Walcott, 1970; Comer *et al.*, 1985]. These flexures are commonly caused by large volcanic loads on the lithosphere which produce a moat and outer rise. On Earth, flexures are also associated with subduction zones; the cold subducted plate applies a bending moment to the not yet subducted lithosphere creating a trench and outer rise [Caldwell *et al.*, 1976]. Despite its high surface temperature (730 K), Venus may also possess an upper elastic lithospheric layer that could deform flexurally. A possible example of flexural deformation on Venus occurs on the North Polar Plains just northward of Freyja Montes where the topography is reminiscent of the outer rise and foredeep of a plate underthrusting a terrestrial mountain range [Solomon and Head, 1990]. The high-resolution radar images and topographic data of Venus obtained by the orbiting Magellan spacecraft have revealed numerous additional examples of possible flexural deformation of the Venusian lithosphere. Prominent among these are the downwarped trenches and outer rises around some coronae as well as interior slopes of large calderalike structures [Sandwell and Schubert, 1991; Solomon *et al.*, 1991; Squyres *et al.*, this issue].

In this paper we focus on flexural signatures outboard of coronal rims with the purpose of inferring the thickness of the Venusian elastic lithosphere. We present topographic profiles [Pettengill *et al.*, 1991; Ford and Pettengill, this issue] outboard of

several prominent coronae which display clear trench and outer rise signatures. Using a thin elastic plate flexure model to characterize the shape of the trench and outer rise, we find that Venusian flexures are similar in both amplitude and wavelength to lithospheric flexures seaward of subduction zones on Earth. Moreover, we show that circumferential fractures are concentrated in areas where the topography is curved downward in good agreement with the high tensile stress predicted by the flexure models. Finally, we present two scenarios for the development of the ridge-trench-outer rise flexural topography and circumferential fractures of coronae. The first scenario involves reheating and thermal subsidence of the lithosphere interior to the corona while the first scenario involves expansion of the corona interior and roll back of the subducting lithosphere exterior to the corona.

FLEXURAL CHARACTERISTICS OF CORONAE

The peripheries of many coronae consist of a relatively narrow annular ridge surrounded by a trench or moat [Barsukov *et al.*, 1986; Basilevsky *et al.*, 1986; Pronin and Stofan, 1990; Stofan and Head, 1990; Solomon *et al.*, 1991; Squyres *et al.*, this issue]. Circumferentially oriented fractures (indicative of radial extension) are often found within the trench and on its exterior wall [Squyres *et al.*, this issue]. Two prominent examples of this ridge/trench signature are Eithinoha and the northern perimeter of Heng-O (Plate 1, top and bottom, respectively). In these images, discrete color changes represent changes in elevation (200 m per color change) and variations in gray level represent the intensity of radar backscatter. This combination enables one to correlate the fractures, apparent in the synthetic aperture radar (SAR) images, with the elevation, slope, and curvature of the surface.

Copyright 1992 by the American Geophysical Union.

Paper number 92JE01274.
0148-0227/92/92JE-01274\$05.00

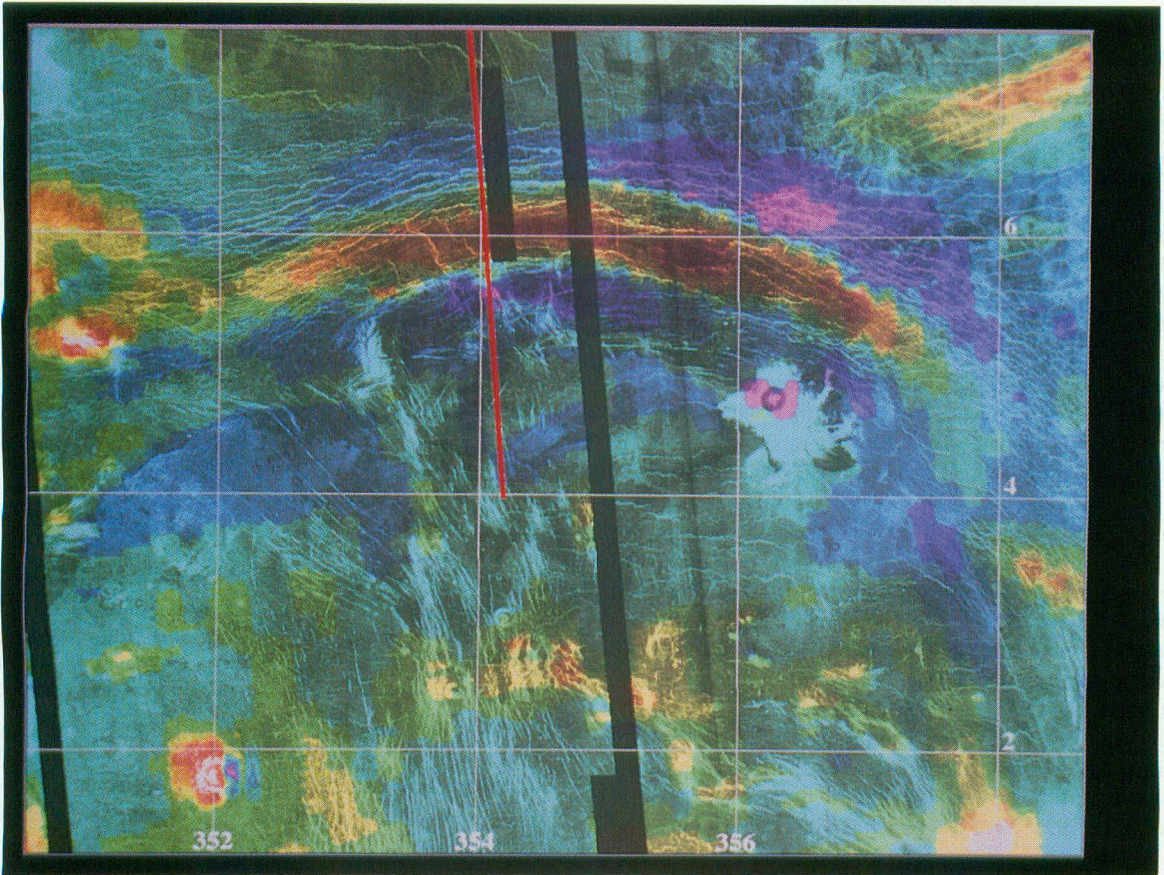
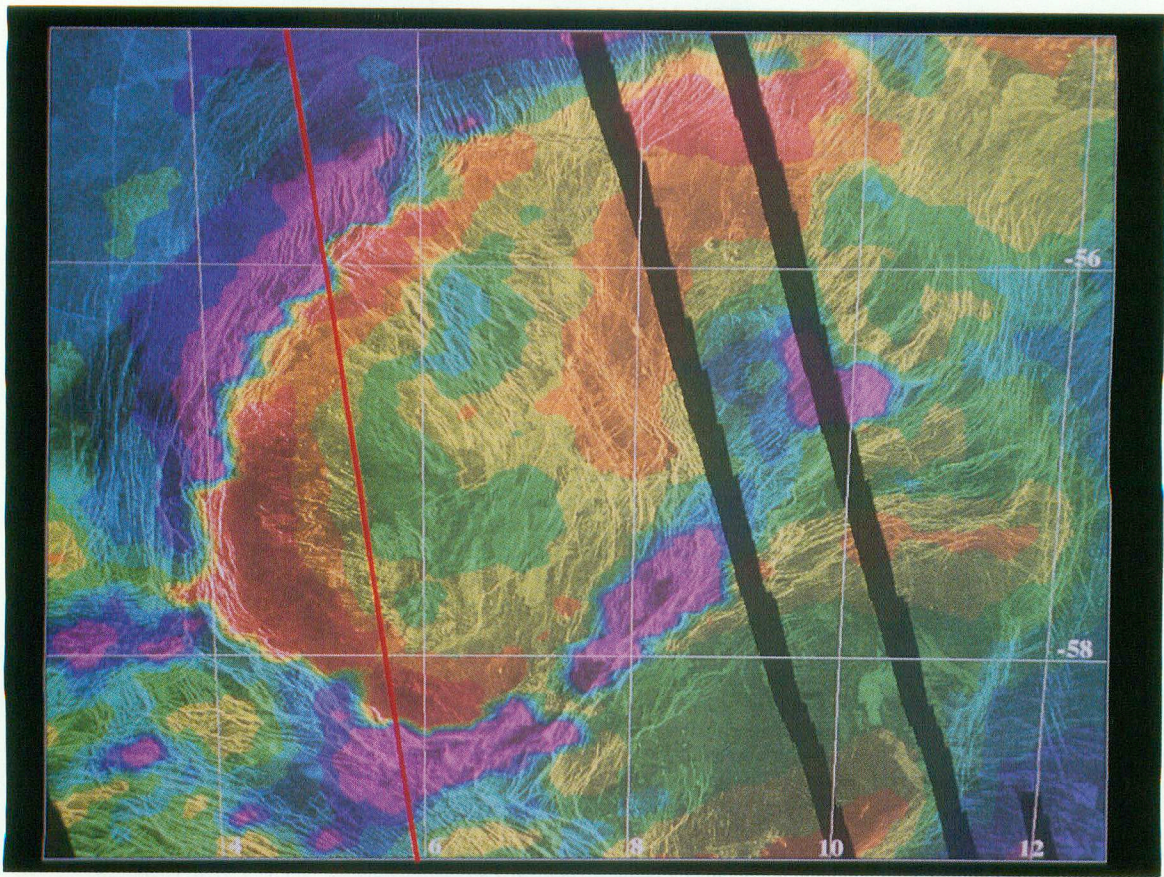


Plate 1. Superposition of SAR image (brightness variations) and topography (color changes each 200 m). Eithinoha (top) is a 400-km-diameter plateau surrounded by ridges and deep trenches. Heng-O is a 1200-km-diameter corona; its northern perimeter (bottom) consists of a ridge, a trench, and an outer rise; circumferential fractures occur in the trench. Dashed line marks locations of profiles in Figure 1.

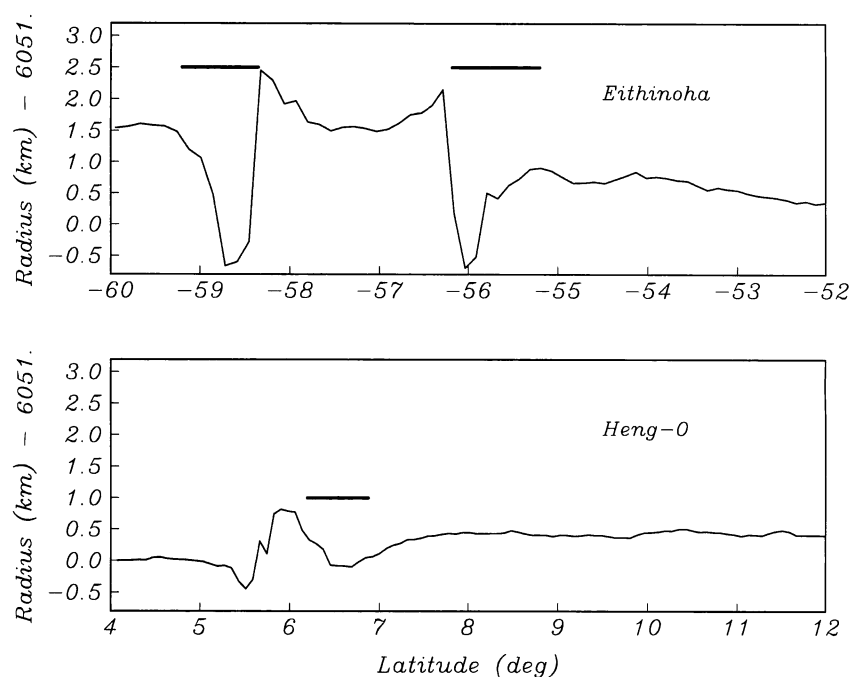


Fig. 1. Topographic profiles across Eithinoha (top) and northern Heng-O (bottom). Track locations are shown in Plate 1. The ridge, trench, and outer rise topography at northern Heng-O is characteristic of lithospheric flexure under a line load. The heavy line above each trench marks the location of the circumferential fractures.

Eithinoha (Plate 1, top), located at 57°S, 8°E, is a plateaulike structure approximately 400 km in diameter. The highly fractured interior of this corona is elevated 0.6-1.0 km with respect to the surrounding plains. Lava flows emanate from the perimeter of the corona and cover some of the fractures on the surrounding plains. A south to north topographic profile (orbit 519) crossing the eastern side of Eithinoha (Figure 1, top) reveals its peripheral ridges and trenches. In this case the trenches are very narrow (~50 km) and the ridges sag toward the center of the corona. The thick horizontal lines above the trenches (Figure 1, top) mark the locations of circumferential fractures apparent in the SAR images. Based on the height of the coronae, its fractured interior, its numerous lava flows, and its lack of impact craters, we speculate that Eithinoha is in a relatively early stage of its thermomechanical and/or tectonic development [Squyres *et al.*, this issue].

Heng-O (~1°N, 355°E) is a much larger corona (~1200 km diameter) with a pronounced ridge-trench-outer rise signature along its northern perimeter as shown in Plate 1 (bottom). The interior of Heng-O lies at approximately the same elevation as the surrounding plains. A topographic profile (orbit 501) crossing its northern rim (Figure 1, bottom), reveals a 1.0-km-tall ridge followed by a 0.5-km-deep trench that is about 80 km wide and a broad outer rise to the north. The circumferential fractures are most intense at the base of the trench and diminish in frequency and intensity moving up out of the trench. Based on the lack of an elevated center, the lack of radar-bright lava flows, and a prominent impact crater in its interior, we speculate that Heng-O is relatively old and has reached a mature stage in its thermomechanical and/or tectonic development.

The largest corona-type feature discovered to date is Artemis [Stofan *et al.*, this issue], located to the south of Aphrodite Terra (at 32°S, 132°E). The dominant characteristic of Artemis is its ridge, trench, and outer rise which form a nearly circular structure approximately 2600 km in diameter. The southeastern part of Artemis is shown in Plate 2 (top) where each color change

represents 400 m of elevation change. The interior of Artemis is elevated by about 1.5 km with respect to the southeastern plains. A topographic profile crossing the southern rim (Figure 2, top, orbit 1191) reveals the elevated interior, a low-broad ridge, a 2.5-km-deep trench and ~1.0-km-high outer rise. The height of the outer rise was measured with respect to the regional topographic gradient which slopes downward to the south. The circumferential fractures, which dominate the SAR images, are confined to the trench and do not extend to the crest of the outer rise. The interior of Artemis contains impact craters and complex fracture patterns [Stofan *et al.*, this issue; McKenzie *et al.*, this issue].

Finally, one of the most striking examples of a ridge-trench-outer rise signature occurs at Latona which is a semicircular structure (~600 km diameter) located on the southern side of Aphrodite (center 22°S, 172°E). The southern part of Latona is shown in Plate 2 (bottom) where each color change represents 400 m of elevation change. The interior of Latona is not a flat plateau but instead consists of two or more topographic ridges that have the morphology of thrust sheets. On average, the interior of Latona lies ~1.5 km above the southeastern plains. A topographic profile crossing the southernmost rim toward the south (Figure 2, bottom, orbit 1376) reveals a 1.5-km-high ridge, a 2.5-km-deep trench, and ~0.5-km-high outer rise. Again, the outer rise was measured with respect to the regional topographic gradient to the south. Circumferential fractures are very intense in the deep part of the trench but decrease in intensity and frequency moving up onto the outer rise where they terminate at the crest of the outer rise. Impact craters are not apparent in the interior of Latona, and since its interior is both elevated and highly fractured, we speculate that Latona is in a relatively early stage of its thermomechanical and/or tectonic development.

A major hypothesis of this paper is that these trenches, outer rises, and circumferential fractures (and perhaps the annular ridges) reflect flexural deformation of the Venusian lithosphere. We test the flexural hypothesis by comparing 53 topographic

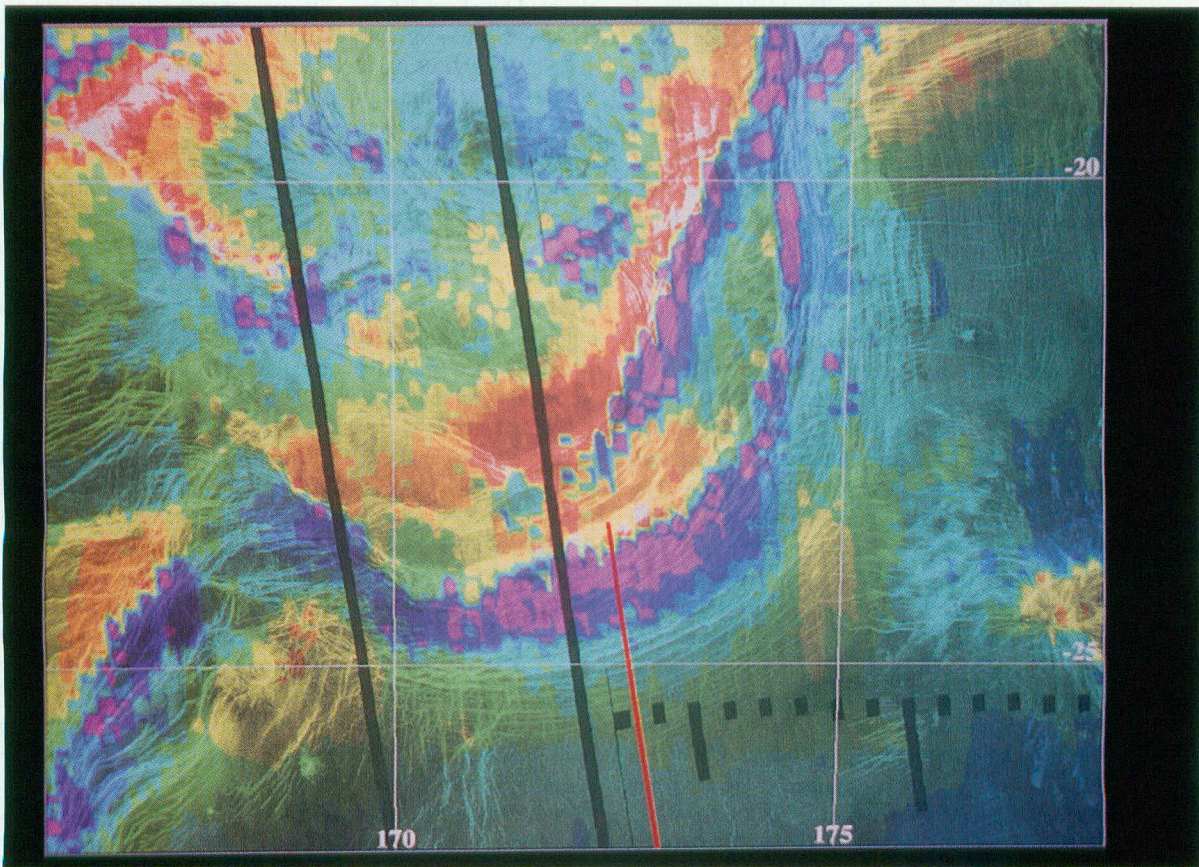
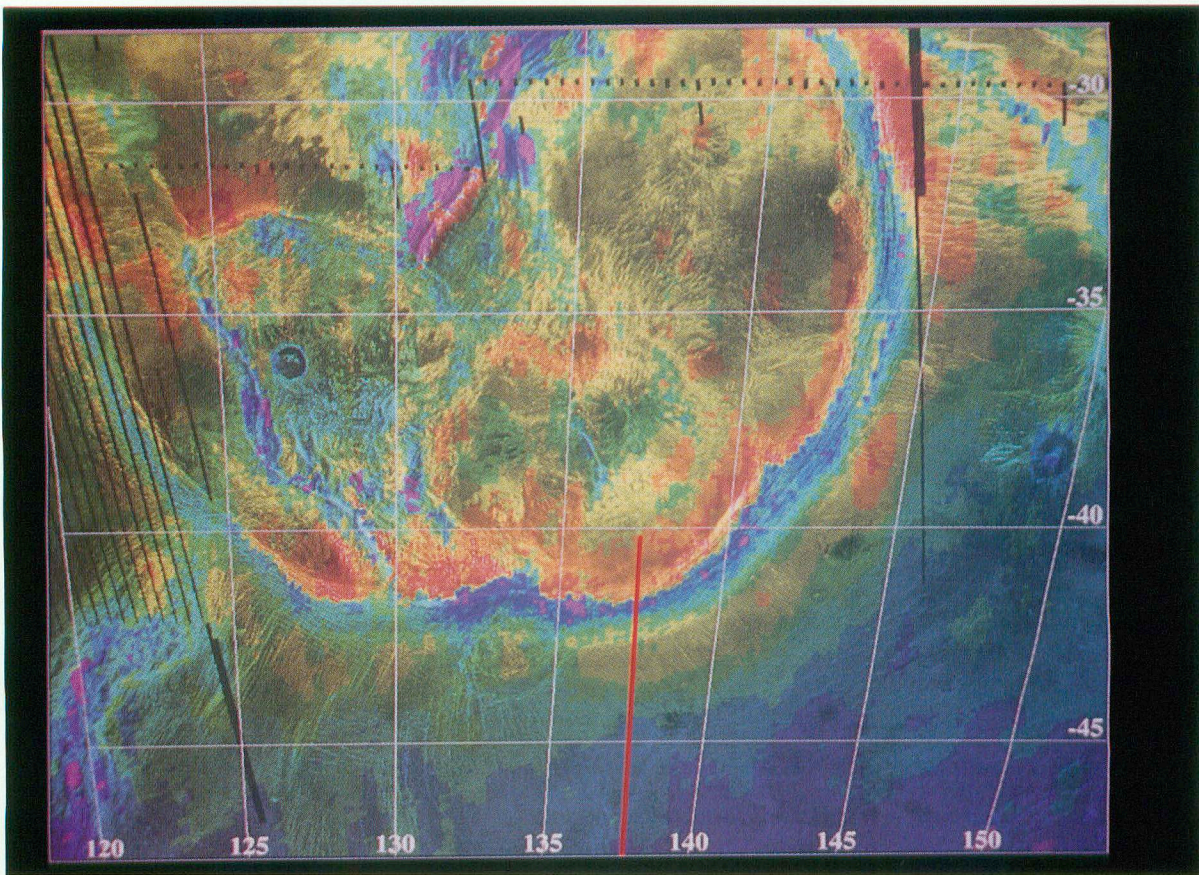


Plate 2. Superposition of SAR image and topography (400 m per color change) for southeastern Artemis (~2600 km diameter) and southeastern Latona (~600 km diameter). In each case, the edge of the plateau has a ridge surrounded by a deep trench. Outer rises occur ~150 km outboard of the trench axis and the trenches contain circumferential fractures. Dashed line marks locations of profiles in Figure 2.

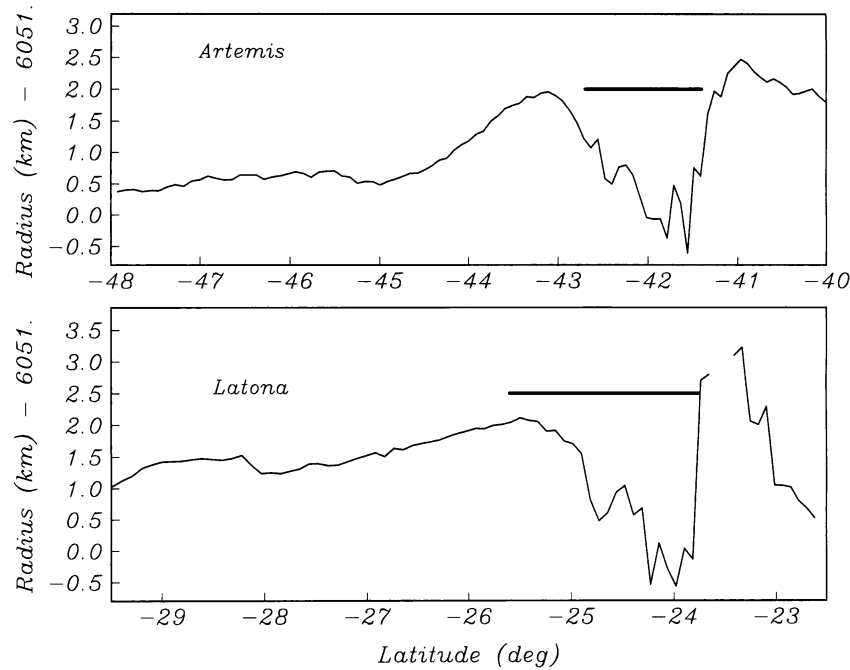


Fig. 2. Topographic profiles across southern Artemis (top) and southern Latona (bottom). Track locations are shown in Plate 2. The heavy line above each trench marks the location of the circumferential fractures. Note the large amplitude ridge, trench and outer rise signatures toward the south.

profiles with the predictions of a simple flexural model. Moreover, the sign and amplitude of the surface stress predicted by the models are compared with the location and intensity of circumferential fractures. We discuss two possible models for the physical causes of the flexure. Other models, e.g., a viscous gravitational relaxation model [Bindschadler and Parmentier, 1990; Stofan *et al.*, 1991; Stofan *et al.*, this issue], may also be able to explain the existence of trenches, outer rises and circumferential fractures.

ESTIMATES OF EFFECTIVE ELASTIC THICKNESS OUTBOARD OF CORONAE

To match the trench and outer rise topography of Eithinoha, Heng-O, Artemis, and Latona, we model the Venusian lithosphere as a thin elastic plate floating on a fluid mantle [Turcotte and Schubert, 1982, pp. 125-131]. The intensity of the circumferential fractures at both Artemis and Latona suggests that the plates are behaving inelastically near the trench axes, and thus a purely elastic model may be inappropriate. Here we follow the procedures applied to Earth trenches which are also believed to be flexed beyond their elastic limits [see Goetze and Evans, 1979; McNutt, 1984]. First, the trench/outer rise topography is fit using a thin elastic plate model. Then the effective elastic thickness and curvature (derived from the elastic model) are used to estimate the inelastic rheology of the lithosphere. For example, on Earth where subducting lithosphere is flexed beyond its elastic limit, the thickness determined from the elastic model is usually only about 75% of the thickness determined using a realistic, layered rheology [McAdoo *et al.*, 1985]. The parameters derived from the elastic model can also be reinterpreted in terms of a purely viscous lithosphere that is subducting at a constant rate [De Bremaecker, 1977; Melosh, 1978]. Thus, while the parameters will be derived from a purely elastic model, they can easily be reinterpreted in terms of nonlinear and viscous rheologies.

The flexure model consists of two components: a bending moment applied to the end of a broken elastic plate and a line load on a continuous elastic plate. A more complicated cylindrically symmetric model was not used because the radii of these features are sufficiently large that the flexural radial topography across the quasi-circular moat of each corona can be approximated by the flexural topography across a linear moat. In addition to the flexural components of the model, a regional trend and mean radius were used. The complete model is

$$w(x) = c_1 \exp\left(\frac{x}{\alpha}\right) \cos\left(\frac{x}{\alpha}\right) + c_2 \exp\left(\frac{x}{\alpha}\right) \left[\cos\left(\frac{x}{\alpha}\right) + \sin\left(\frac{x}{\alpha}\right) \right] + c_3 x + c_4 \quad (1)$$

where x is horizontal distance perpendicular to the strike of the trench, c_1 (km) is the coefficient of the bending moment term, c_2 (km) is the coefficient of the line load term, c_3 (km/km) is the regional topographic gradient, c_4 (km) is the radius, and α (km) is the flexural parameter given by

$$\alpha = \left[\frac{E h^3}{3 \rho g (1 - \nu^2)} \right]^{1/4} \quad (2)$$

In (2), E is Young's modulus, ν is Poisson's ratio, ρ is mantle density, g is acceleration of gravity, and h is the unknown thickness of the elastic plate. Values of constant parameters are given in Table 1. After fitting the topographic profiles using (1), we calculate the bending moment M and surface stress σ_{xx} (positive is tension) along the flexed lithosphere. These two quantities are given by

$$M(x) = -D \frac{d^2 w}{d x^2} \quad (3)$$

$$\sigma_{xx} = \frac{6 M}{h^2} \quad (4)$$

TABLE 1. Thermal and Mechanical Parameter Values for Venusian Lithosphere

Parameter	Value
T_m , mantle temperature	1673 K
T_e , temperature at base of elastic lithosphere	1023 K
T_o , surface temperature	728 K
α , thermal expansivity	$3.1 \times 10^{-5} \text{ K}^{-1}$
E , Young's modulus	65 GPa
ρ_m , mantle density	3000 kg m^{-3}
κ , thermal diffusivity	$8 \times 10^{-7} \text{ m}^2 \text{ s}^{-1}$
ν , Poisson's ratio	0.25
g , acceleration of gravity	8.87 m s^{-2}

where D is the flexural rigidity given by

$$D = \left[\frac{E h^3}{12(1 - \nu^2)} \right] \quad (5)$$

To compare the flexure models of Venusian lithosphere with flexure models of subducting lithosphere on Earth, the bending moment M_o and plate curvature K_o at the first zero crossing seaward of the trench axis x_o are calculated. The first zero crossing is found by setting the flexure part of (1) equal to zero and solving for the first nonnegative position

$$\frac{x_o}{\alpha} = \tan^{-1} \left[\frac{-(c_1 + c_2)}{c_2} \right] + \pi \quad (6)$$

The objective is to estimate the flexural parameter α and the flexural coefficients c_1 and c_2 by varying all of the parameters (α , c_1 , c_2 , c_3 , c_4) such that the root-mean-square (RMS) misfit between the model and the observations is minimum. After determining α , c_1 , and c_2 we estimate the elastic plate thickness using (2) and the maximum bending moment which occurs at the base of the trench using (3).

While this is the standard least squares approach, there are a number of complications arising from this application. First, one may notice that there is no obvious adjustable parameter to specify the location of the origin in (1). The approximate position of the origin was chosen as the highest point along the ridge just inboard of the trench axis since this is where the line load and bending moment are acting; in fact, the highest point was selected after the profile was low-pass-filtered (~ 160 -km cutoff wavelength) in order to smooth out local maxima/minima superimposed on the broader ridge. In addition to having the origin coincide with the peak in the topographic load, the location of the origin was allowed to vary to achieve a "best fit" to the observations. These minor variations are accommodated by varying the relative amplitudes of c_1 and c_2 which contain cosine and sine terms that shift the phase of the flexure profile.

After specifying the origin, the latitude and longitude of the profile were converted to distance perpendicular to the trench axis. To focus on the trench and outer rise flexure, only the observations at distances of ~ 100 to ~ 600 km were used in the least squares fit. As seen in (1), the model depends linearly on the parameters $c_1 - c_4$ but nonlinearly on α . To determine the model with the minimum RMS misfit, we set α and found the best set of $c_1 - c_4$. This procedure was repeated for a wide range of α corresponding to elastic thicknesses of 5 to 80 km. One more complication arose because the observations do not continue all the way to the origin (i.e., the topographic ridge adjacent to the trench). When the flexural parameter was much less than the distance from the origin

to the trench axis, the best coefficients of the end moment and line load (c_1 and c_2) would act in opposite directions to create a nice fit to the observations in the 100 to 600 km distance range. However, at the origin, the model topography would have an unrealistic value ($> \pm 100$ km). To suppress this instability, we forced both c_1 and c_2 to be negative [Lawson and Hanson, 1974]; physically, this constrains both the end moment and line load to flex the plate downward at the origin.

Freyja Montes

We tested the procedure using seven profiles (even numbered orbits 500-512) across northern Freyja Montes (80°N , 335°E) where Solomon and Head [1990] modelled a trench and outer rise signature using three Venera 15 and 16 altimeter profiles. An example of the fits of models having five elastic thicknesses (0, 10, 20, 30, and 40 km) to profile 506 are shown in Figure 3 (bottom). The 0 km elastic thickness corresponds to a model consisting of only a linear trend (i.e., only c_3 and c_4 in (1)). The model with the 10-km-thick elastic plate flexes too sharply to match the outer rise while the 40-km flexure model does not bend sharp enough. A 20-km-thick plate provides the best fit. The surface stress (positive tension) predicted by the best model is also shown in Figure 3 (top). The surface tensile stress is greatest at about 60 km from the origin where the plate curvature is maximum.

The best fitting models for all seven profiles are shown in Figure 4, and the misfits and coefficients $c_1 - c_3$ are given in Table 2. The bending moment M_o and plate curvature K_o at the first zero

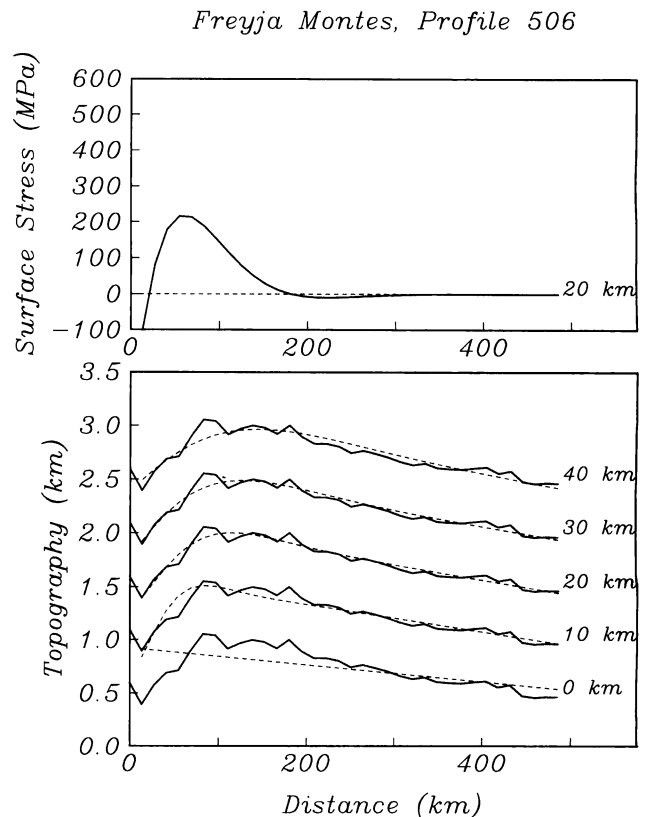


Fig. 3. Fits of plate flexure models to profile 506 across northern Freyja Montes (bottom). The 20-km-thick elastic plate provides the minimum RMS fit as well as the best visual fit. Model surface stress is tensile between the trench axis and ~ 170 km (top).

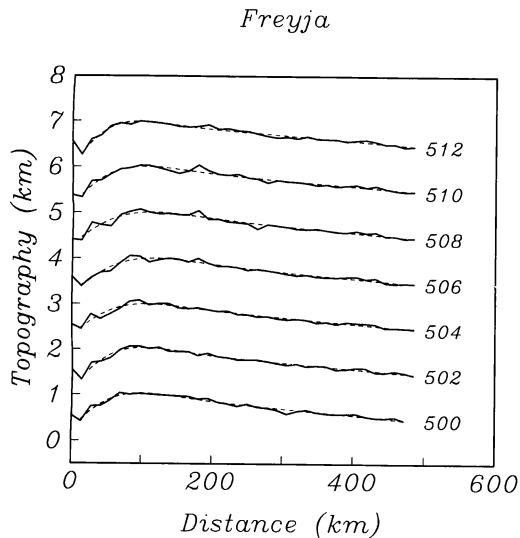


Fig. 4. Best fits of flexure model to seven profiles across northern Freyja Montes (even numbered orbits 500-512). Best fit model parameters are given in Table 2.

crossing outboard of the trench axis are also given in Table 2 for later comparison with trenches on Earth. A plot of RMS misfit for all seven profiles versus elastic thickness (Figure 5) reveals a sharp decrease in misfit between thicknesses of 0 and 10 km. The minimum misfit occurs at an elastic thickness of about 18 km, although models with elastic thicknesses ranging from about 10 to 25 km fit the data fairly well. This is in good agreement with the 11-18 km elastic thickness range found by *Solomon and Head* [1990] using a different data set and a different method.

Eithinoha

The same modelling procedures were applied at Eithinoha, Heng-O, Artemis, and Latona. An example of the fits of models having five elastic thicknesses (0, 4, 12, 20, and 28 km) to profile 519 crossing the northern perimeter of Eithinoha is shown in Figure 6 (bottom). In this case, an 8-km-thick elastic plate flexes too sharply, while plates thicker than 28 km do not bend sharply enough; a 12-km-thick plate provides the best fit to this profile. The tensile surface stress for the 12-km-thick model (Figure 6, top) is moderate between 50 km and 100 km from the origin. Circumferential fractures occur from the origin out to about 75 km (thick line) in fair agreement with the model.

The best fitting models for all four profiles across northern Eithinoha are shown in Figure 7. Models having elastic thicknesses between 10 and 30 km all fit the data fairly well although the best fitting model has an elastic thickness of about 15 km. While Eithinoha does not provide the strongest evidence for lithospheric flexure, it does provide an example of a relatively thin elastic plate to contrast with other areas having thick plates.

Heng-O

An example of the fits of models having five elastic thicknesses (0, 20, 30, 40, and 50 km) to profile 501 crossing the northern perimeter of Heng-O is shown in Figure 8 (bottom). In this case a 20-km-thick plate flexes too sharply, while all plate thicknesses greater than 30 km match the profile fairly well. For Heng-O, the

RMS misfit does not decrease significantly for plates thicker than 40 km (Figure 5) so we have adopted this as the best plausible value. The tensile surface stress for the 40-km-thick model (Figure 8, top) is moderate between 50 km and 200 km from the origin. Circumferential fractures occur from the origin out to about 110 km (thick line) in fair agreement with the model.

The best fitting models for all 15 profiles across northern Heng-O are shown in Figure 9. In contrast to Freyja and Eithinoha which require elastic plate thicknesses greater than 10 km, Heng-O requires an elastic plate thickness that is greater than 30 km (Figure 5). This can be seen in Figure 8 where the fit of the 20-km-thick model is quite poor on the outer trench wall. It is interesting to note that the amplitude and shape of the flexure at Heng-O do not place tight constraints on the maximum elastic plate thickness. In fact, for most of the profiles, the minimum RMS misfit occurred for an elastic plate thickness of 80 km. A visual examination of the fits of these profiles, however, showed a poor match at the base of the trench. Therefore, the results shown in Figure 9 and given in Table 2 are best fitting models having elastic thickness less than or equal to 40 km.

Artemis

The amplitude of the flexure at Artemis is extremely large. This high amplitude combined with a peaked outer rise provides a tight constraint on the acceptable values of elastic thickness. For example, the large-amplitude flexure along profile 1191 is well matched by a 30-km-thick elastic plate, while plate thicknesses of 20 km and 50 km are unacceptable (Figure 10, bottom). The fits to all 12 profiles at Artemis are remarkably consistent (Figure 11). The best overall model has an elastic thickness of 37 km, while the range of acceptable elastic thicknesses lies between 30 km and 45 km (Figure 5). Models with elastic thicknesses of 25 km or less are incompatible with the observations.

The surface stress predicted by the 30-km-thick elastic plate model (Figure 8, top) exceeds 1.0 GPa. This stress is too large to be sustained by even the strongest rocks at high confining pressures (40 km deep) [*Goetze and Evans*, 1979]. The implication is that the lithosphere between the origin and 200 km has undergone complete failure. The plate is bent beyond its elastic limit, and the magnitude of the stress is limited by the strength of the rock. Note that this zone of extremely high stress approximately coincides with the location of the intense surface fractures (thick line). The flexure model also predicts less intense surface fractures on the crest of the outer rise where circumferential fractures are not seen. This combination of tall outer rise and lack of evidence for tensile stress on the outer rise can also be explained by a flexure model that incorporates a significant component of radial compression. However, since a bending moment and an end load produce similar topographic signatures [*Parsons and Molnar*, 1976], evidence for compression is inconclusive.

Latona

The amplitude of the flexure at the southern perimeter of Latona is also quite large and places a tight constraint on the range of acceptable elastic thicknesses. For example, profile 1376 is best modelled using a 30-km-thick elastic plate while plate thicknesses of 20 km and 50 km are unacceptable (Figure 12, bottom). Indeed the best solution for the 20-km-thick plate is just a straight line. The fits to all 15 profiles at Latona are again remarkably consistent (Figure 13). The best overall model has an elastic thickness of 35

TABLE 2. Trench Profile Models

	Orbit	h , km	Best RMS, m	Line RMS, m	c_1 km	c_2 , km	c_3 , 10^{-3}	M_0 , 10^{16} N	K_0 10^{-8}m^{-1}
Freyja	0500	20	35.8	131.1	-0.866		-1.465	0.63	13.66
Freyja	0502	20	35.6	144.7	-0.972		-1.401	0.70	15.34
Freyja	0504	20	44.3	139.9	-0.656	-0.142	-1.402	0.49	0.72
Freyja	0506	20	39.5	140.8	-0.562	-0.326	-1.456	0.48	10.50
Freyja	0508	25	55.1	145.5	-0.825		-1.441	0.84	9.31
Freyja	0510	20	44.7	77.6	-0.901	-0.019	-1.309	0.65	14.22
Freyja	0512	15	33.9	83.1	-0.729	-0.278	-1.287	0.37	19.39
Eithinoha	0515	24	100.8	162.2	-1.332	-0.133	-2.602	1.28	16.12
Eithinoha	0517	20	72.2	209.2	-0.414	-1.406	-2.021	0.86	18.80
Eithinoha	0519	16	109.0	227.0	-1.399	-1.418	-1.608	1.03	43.61
Eithinoha	0521	12	91.6	165.4		-2.081	-1.296	0.45	45.53
Heng-O	0495	40	36.7	109.9	-0.652	-0.242	*	1.46	3.96
Heng-O	0496	40	34.7	139.8		-0.539	*	0.71	1.93
Heng-O	0497	40	51.6	144.8		-0.622	*	0.82	2.23
Heng-O	0498	40	67.7	128.8		-0.789	*	1.04	2.83
Heng-O	0499	40	85.5	126.4		-0.755	*	1.00	2.71
Heng-O	0500	35	46.4	113.1		-0.918	*	1.00	4.03
Heng-O	0501	35	34.9	118.1		-0.931	*	1.01	4.09
Heng-O	0502	35	39.3	125.9		-0.806	*	0.87	3.54
Heng-O	0503	40	31.9	115.2		-0.738	*	0.98	2.65
Heng-O	0504	40	40.2	102.7		-0.693	*	0.92	2.49
Heng-O	0505	40	45.5	118.1		-0.613	*	0.81	2.20
Heng-O	0506	40	38.8	132.6		-0.548	*	0.72	1.97
Heng-O	0507	40	34.9	148.9	-0.061	-0.696	*	1.00	2.72
Heng-O	0508	40	31.5	230.6		-0.911	*	1.21	3.27
Heng-O	0509	40	40.1	215.1		-0.999	*	1.32	3.59
Artemis	1183	35	137.1	221.3	-10.936	-2.264	-0.860	19.07	76.99
Artemis	1185	30	109.2	222.0	-8.851	-5.058	-1.221	13.98	89.65
Artemis	1187	30	113.5	243.3	-6.774	-7.934	-1.359	13.64	87.49
Artemis	1189	30	109.9	253.2	-7.798	-10.177	-1.323	16.52	105.95
Artemis	1191	30	78.5	249.1	-7.301	-15.404	-1.182	20.24	129.78
Artemis	1193	30	86.3	260.6	-2.863	-19.236	-1.258	19.17	122.90
Artemis	1195	35	61.2	284.7	-12.910	-8.267	-1.082	26.44	106.75
Artemis	1197	35	40.2	289.9	-16.189	-4.513	-0.925	28.85	116.47
Artemis	1199	35	55.6	267.4	-18.003	-3.147	-0.894	31.13	125.68
Artemis	1201	40	65.6	290.5	-17.869	-5.769	-0.868	39.49	106.80
Artemis	1203	45	60.9	167.9	-16.455	-5.867	-0.994	43.92	83.41
Artemis	1205	40	58.4	221.6	-6.766	-16.952	-1.234	32.32	87.41
Latona	1370	30	95.0	236.6	-0.933	-5.153	-2.137	5.29	33.91
Latona	1371	35	102.5	270.6	-0.439	-5.434	-2.491	6.40	25.84
Latona	1372	35	99.1	278.4	-0.466	-5.132	-2.241	6.10	24.64
Latona	1373	30	102.9	252.6		-9.109	-1.996	7.86	50.43
Latona	1374	30	129.9	327.8		-8.369	-1.965	7.22	46.33
Latona	1375	30	102.5	242.4		-7.775	-2.062	6.71	43.04
Latona	1376	30	162.0	200.2		-9.004	-1.795	7.77	49.84
Latona	1377	30	138.9	214.2		-6.144	-2.022	5.30	34.01
Latona	1378	30	125.6	295.4		-5.711	-2.189	4.93	31.61
Latona	1379	35	96.5	190.6	-0.477	-3.586	-2.238	4.43	17.92
Latona	1380	35	126.3	264.1		-5.881	-2.109	6.40	25.83
Latona	1381	40	92.0	230.6	-0.549	-2.967	-2.160	4.70	12.73
Latona	1382	40	86.1	309.2		-4.186	-2.100	5.56	15.05
Latona	1383	40	82.7	230.6	-0.454	-3.714	-2.060	5.56	15.03
Latona	1384	45	126.4	325.7		-4.142	-1.972	6.57	12.48

Maximum elastic thickness for Heng-O was set to 40 km.

Line RMS corresponds to 0-km elastic thickness.

*The gradient parameter was not included in fits to Heng-O.

km, while the range of acceptable elastic thicknesses lies between 27 km and 60 km (Figure 5). As in the case of Artemis, models with elastic thicknesses of 25 km or less are incompatible with the observations. For profile 1376 (Figure 12, top) the surface tensile

stress is greatest in the deep part of the trench and diminishes moving up onto the crest of the outer rise (Figure 2). There is an excellent correlation between stress intensity and surface fracturing.

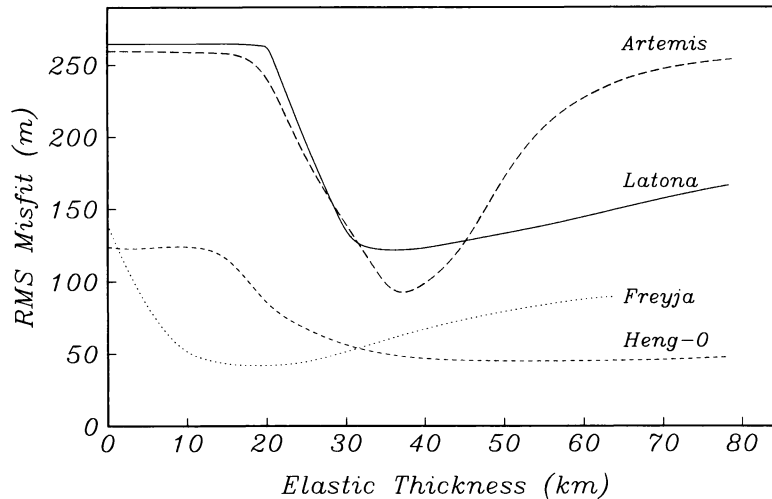


Fig. 5. RMS misfit of flexure model versus elastic plate thickness for seven profiles across northern Freyja Montes, four profiles across northern Eithinoha, 15 profiles across northern Heng-O, 12 profiles across southern Artemis, and 15 profiles across southern Latona. Zero elastic thickness corresponds to a linear trend model with no flexure. The minimum of each misfit curve provides an estimate of the elastic plate thickness (~18 km, Freyja; ~15 km, Eithinoha; ~37 km, Artemis; 35 km, Latona; Heng-O has no minimum).

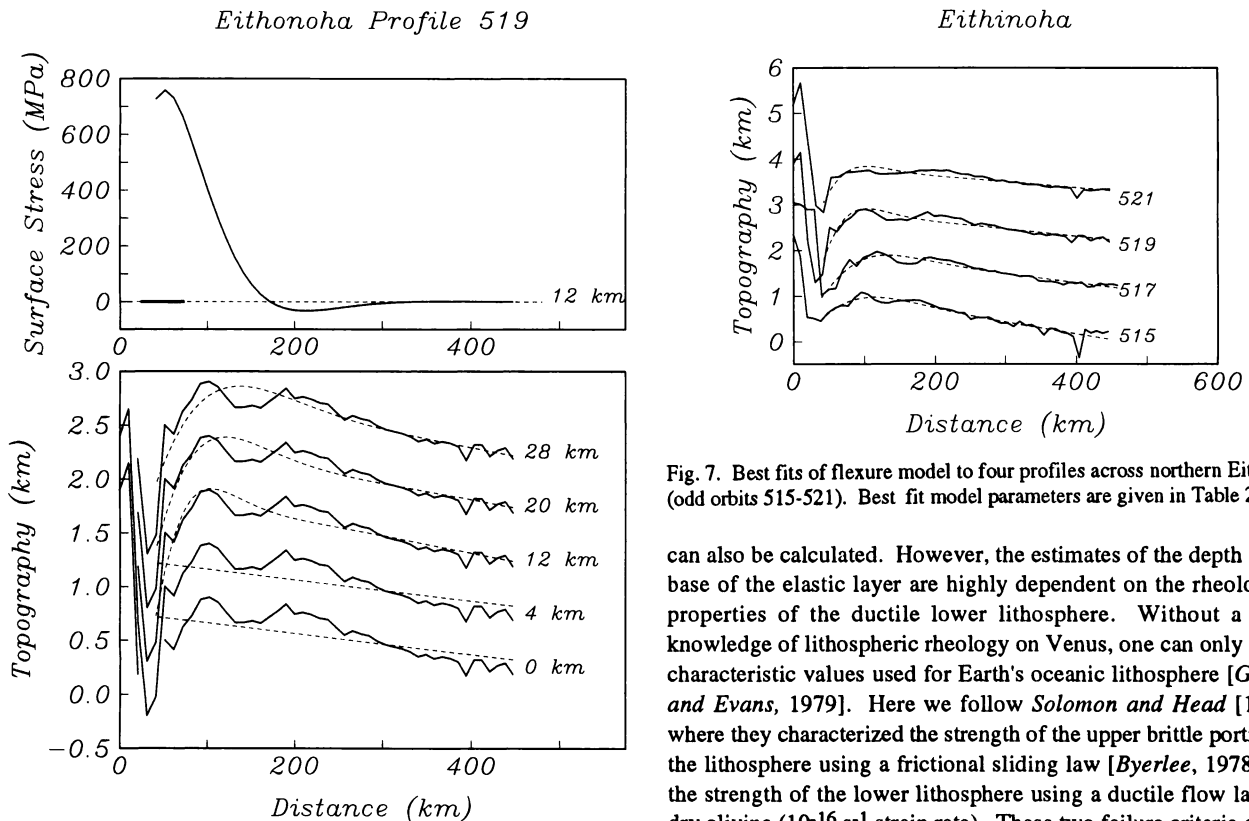


Fig. 6. Fits of plate flexure models to profile 519 across northern Eithinoha (bottom). The 12-km-thick elastic plate provides the minimum RMS fit as well as the best visual fit. Model surface stress is tensile between the trench axis and ~150 km (top). Circumferential fractures (thick line, top) occur out to a distance of 75 km.

LITHOSPHERIC THERMAL GRADIENT

The parameters of the best fitting thin elastic plate models can be used to estimate the depth to the base of the elastic layer. Assuming this corresponds to an isotherm, the geothermal gradient

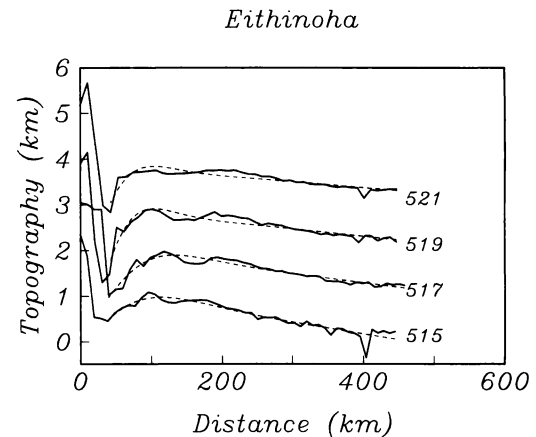


Fig. 7. Best fits of flexure model to four profiles across northern Eithinoha (odd orbits 515-521). Best fit model parameters are given in Table 2.

can also be calculated. However, the estimates of the depth to the base of the elastic layer are highly dependent on the rheological properties of the ductile lower lithosphere. Without a good knowledge of lithospheric rheology on Venus, one can only adopt characteristic values used for Earth's oceanic lithosphere [Goetze and Evans, 1979]. Here we follow Solomon and Head [1990] where they characterized the strength of the upper brittle portion of the lithosphere using a frictional sliding law [Byerlee, 1978] and the strength of the lower lithosphere using a ductile flow law for dry olivine (10^{-16} s $^{-1}$ strain rate). These two failure criteria define a yield strength envelope (YSE) [Goetze and Evans, 1979] where the base of the YSE is approximately defined by the 740 K isotherm [McAdoo et al., 1985] and the thickness of the YSE is the mechanical thickness of the lithosphere.

When the lithosphere is flexed, the largest deviatoric stresses occur at the top and bottom of the layer. For moderate plate curvatures ($\sim 10^{-7}$ m $^{-1}$), significant yielding occurs in both the uppermost and lowermost part of the mechanical lithosphere which are weak. This yielding causes the effective elastic thickness of the lithosphere (i.e., derived from flexure modelling) to be less than the actual mechanical thickness of the lithosphere McNutt [1984].

Heng-0, Profile 501

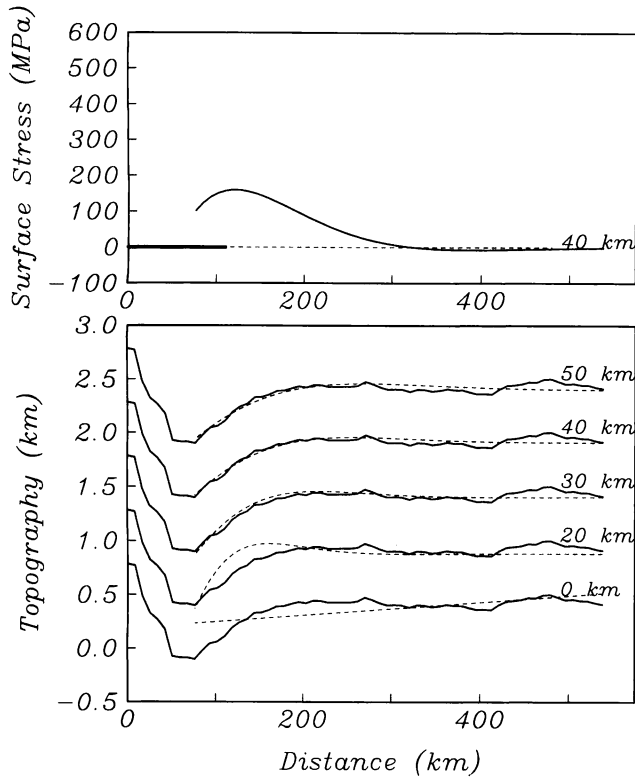


Fig. 8. Fits of plate flexure models to profile 501 across northern Heng-O (bottom). The 40-km-thick elastic plate provides the minimum RMS fit as well as the best visual fit. Model surface stress is tensile between the trench axis and ~300 km (top). Circumferential fractures (thick line, top) occur out to a distance of 160 km.

Artemis, Profile 1191

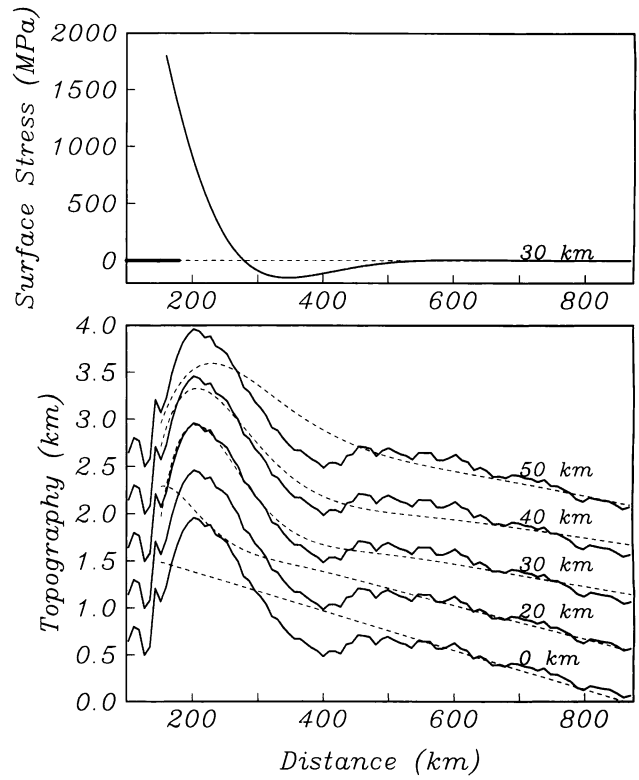


Fig. 10. Fits of plate flexure models to profile 1191 across southern Artemis (bottom). The 30-km-thick elastic plate provides the minimum RMS fit as well as the best visual fit. Model surface stress is tensile between the trench axis and ~280 km (top). Circumferential fractures (thick line, top) occur out to a distance of 180 km.

Heng-0

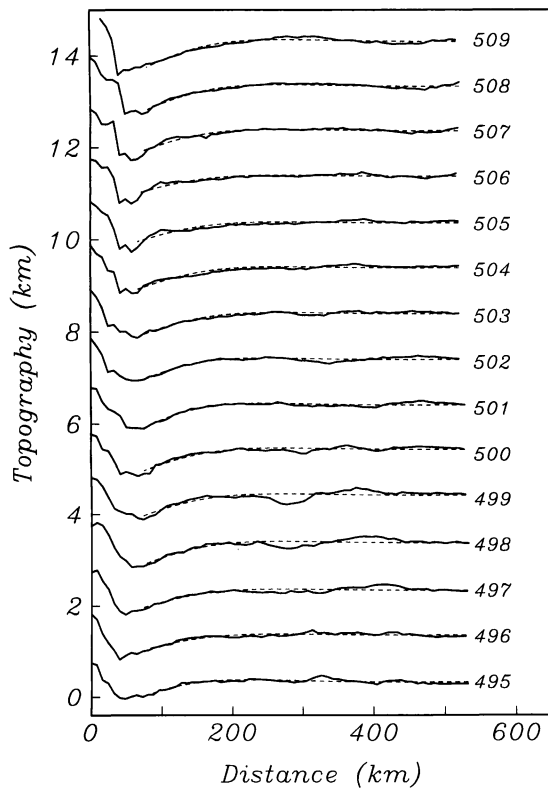


Fig. 9. Best fits of flexure model to 15 profiles across northern Heng-O (orbits 495-512). Best fit model parameters are given in Table 2.

Artemis

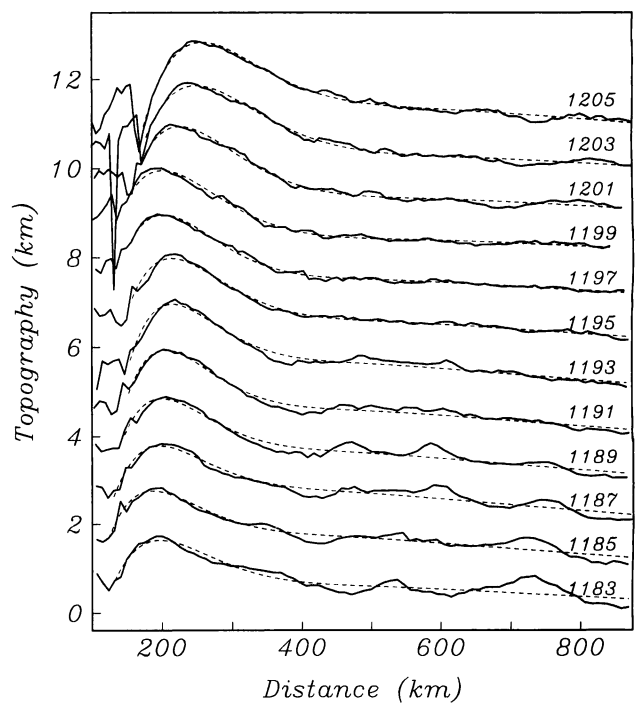


Fig. 11. Best fits of flexure model to 12 profiles across southern Artemis (odd numbered orbits 1183-1205). Best fit model parameters are given in Table 2.

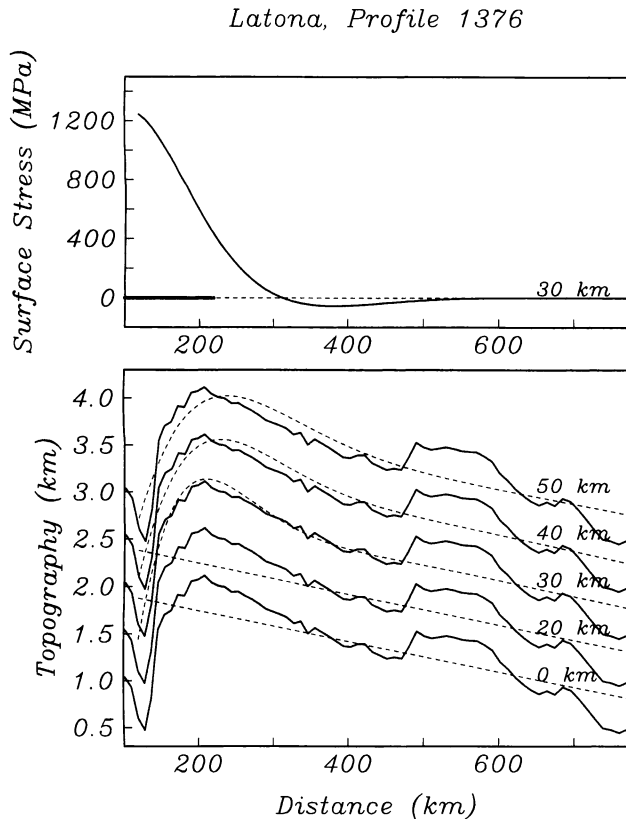


Fig. 12. Fits of plate flexure models to profile 1376 across southern Latona (bottom). The 30-km-thick elastic plate provides the minimum RMS fit as well as the best visual fit. Model surface stress is tensile between the trench axis and ~ 300 km (top). Circumferential fractures (thick line, top) occur out to a distance of 230 km.

Complete lithospheric failure occurs when the plate curvature exceeds about 10^{-6} m^{-1} . (Note that Artemis has an average plate curvature of 10^{-6} m^{-1} , suggesting that the lithosphere has failed.) *Solomon and Head* [1990] adapted this YSE model for the parameters appropriate to Venus and provide a diagram to map the elastic thickness into mechanical thickness by using the plate curvature (Figure 4 of their paper). We have used their diagram with our estimates of elastic thickness and plate curvature (Table 2) to estimate the mechanical thickness of the lithosphere outboard of Freyja, Heng-O, Artemis, and Latona; the results are given in Table 3.

At Freyja Montes, we find the best range of elastic thicknesses is between 10 and 25 km and the plate curvature is $13 \times 10^{-8} \text{ m}^{-1}$; this agrees well with *Solomon and Head's* [1990] estimates based on Venera 15 and 16 altimeter profiles. These parameters map into thermal gradients of between 9.5 and 26 K/km. A similar range of thermal gradient is inferred at Eithinoha (6.8–24 K/km). For the other three areas, however, we estimate that the mechanical thickness of the lithosphere is greater than 30 km (Table 3) which maps into much lower thermal gradients (< 10 K/km).

Assuming the Venusian lithosphere has a thermal conductivity of $3.3 \text{ W m}^{-1} \text{ K}^{-1}$, the temperature gradients estimated at Heng-O, Artemis, and Latona correspond to a surface heat flow of less than 33 mW m^{-2} . This is less than one half of the expected planetary average heat flow for Venus. There are many possible explanations for this low estimate: (1) The lithosphere on Venus remains strong at temperatures exceeding 1013 K (740°C) or the strain rates are much higher than on the Earth. (2) The thermal

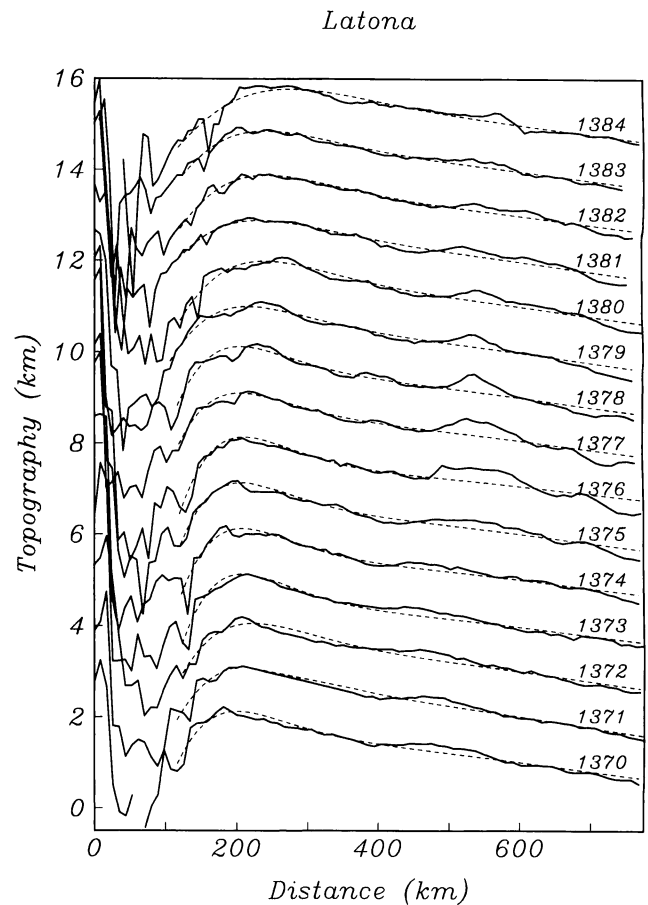


Fig. 13. Best fits of the flexure model to 15 profiles across southern Latona (orbits 1370–1384). Best fit model parameters are given in Table 2.

conductivity used in the above calculation is too low. (3) The areas that we have investigated have anomalously thick and strong lithospheres with respect to the average lithospheric thickness on Venus. (4) The heat production in the interior of Venus is substantially lower than the heat production inside Earth. (5) Venus loses a substantial fraction of its heat by extrusion of large quantities of lava. (6) Heat loss on Venus is episodic and global with a time scale > 200 m.y. Over the next few years it will be important to eliminate as many of these explanations as possible to arrive at a better understanding of the Venusian heat loss budget. At this time it would be premature to speculate on the most likely explanation, however.

TECTONIC AND THERMAL MODELS FOR THE DEVELOPMENT OF A RIDGE, TRENCH, AND OUTER RISE

We propose two models (scenarios) for the development of ridge, trench, and outer rise flexural topography on the perimeters of the largest coronae. In the first model (Figure 14, tectonic scenario), a mantle plume reaches the base of the lithosphere and spreads horizontally (i.e., radially) outward beneath the underside of the lithosphere. The hot, light plume forms an inverted pancake that is held up against the bottom of the lithosphere by virtue of its buoyancy. Over time this hot plume head thins and weakens the lithosphere. Melt penetrates the lithosphere providing a route for further escape of hot mantle material. A large volume of mantle material spreads over the top surface of the lithosphere causing it to depress and ultimately to fracture and fail. The cold lithosphere on

TABLE 3. Lithospheric Thickness and Temperature Gradient

	Elastic Thickness, km	Curvature, 10^{-8} m^{-1}	Mechanical Thickness,* km	Temperature Gradient,+ K km^{-1}
Freyja#	11 - 18	15	12 - 21	24 - 14
Freyja	10 - 25	13	11 - 30	26 - 9.5
Eithinoha	10 - 30	29	12 - 42	24 - 6.8
Heng-O	30 - 45	3	32 - 49	8.9 - 5.8
Artemis	30 - 45	103	60 - 90	4.8 - 3.2
Latona	27 - 60	29	37 - 82	7.7 - 3.5

*Mechanical thickness derived from Figure 4. of *Solomon and Head* [1990].

+Temperature gradient based on 1013 K (740°C) temperature at base of elastic layer.

Published results, *Solomon and Head* [1990].

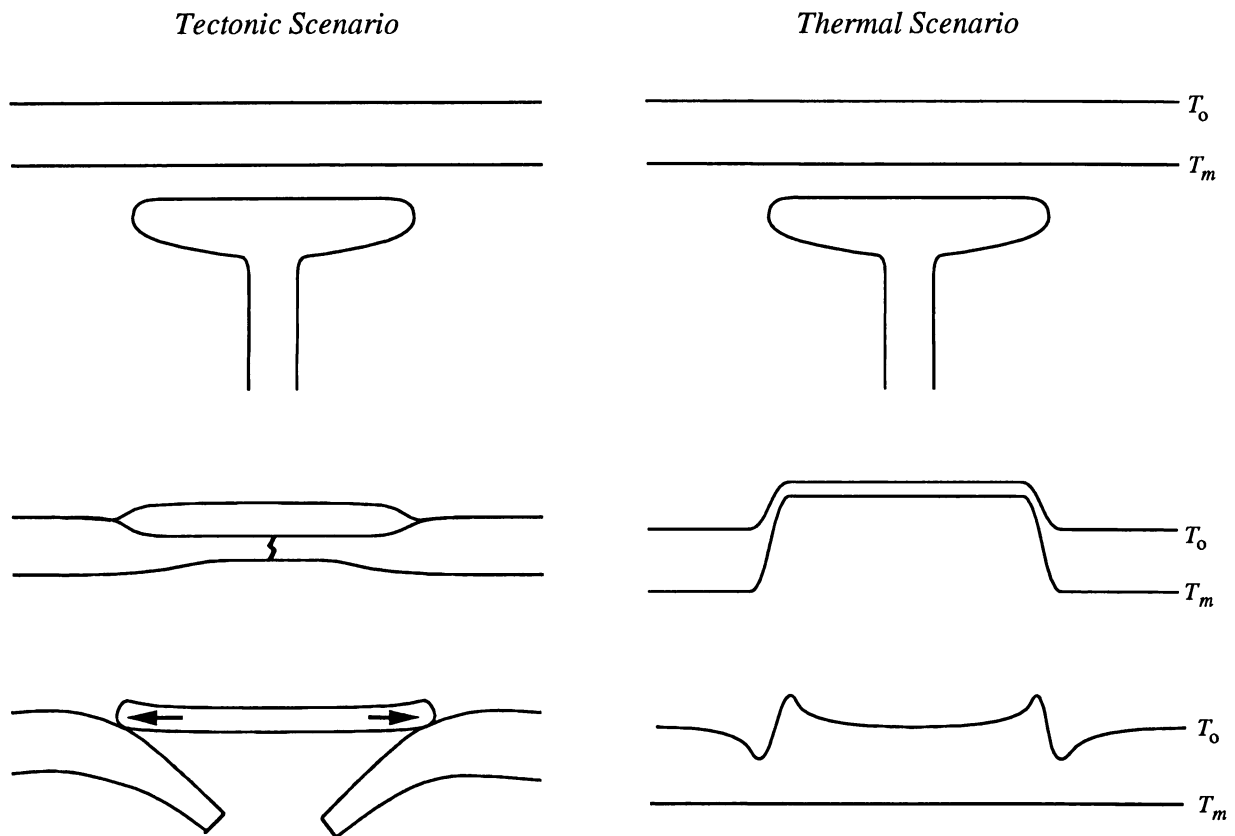


Fig. 14. (Left) Tectonic scenario: plume head approaches the lithosphere and spreads radially, causing it to thin and weaken; melt and hot mantle material pond on the surface of the lithosphere causing it to fail under the load; the old and dense lithosphere sinks into the mantle forming a circular subduction zone that increases in radius with time; the interior spreads radially to fill the growing void; a prominent trench and outer rise develop. (Right) Thermal scenario: plume head approaches the lithosphere and spreads radially; thermal conduction and/or advection thins the lower lithosphere in a circular area with sharp edges; the hot interior cools and subsides relative to the cool exterior forming ridge, trench, and outer rise topography.

the perimeter of the flow sinks into the mantle forming a subduction zone and circumferential fractures (i.e., a corona). Continued subduction causes the trench to roll back so the radius of the corona increases and the interior of the corona expands to fill the void. This type of subduction and back arc spreading is commonly found behind subduction zones on Earth.

In the second model (Figure 14, thermal scenario) a mantle plume head also reaches the base of the lithosphere and spreads horizontally (i.e., radially) outward. As in the first model, the hot, light plume forms an inverted pancake that is held up against the

bottom of the lithosphere by virtue of its buoyancy. However, this time only a smaller volume of melt escapes to the surface. The hot material in the plume thins the lithosphere and creates an isostatically compensated plateau at the surface. As shown below, the transition from the hot-thin interior to the cold-thick exterior must be quite sharp (<50 km) for a ridge/trench signature to develop. The interior lithosphere then cools to the surface, while the exterior lithosphere maintains its temperature profile through a balance of heat supply at its base with heat loss at its surface. As a consequence of the cooling, the interior lithosphere increases in

density and it subsides isostatically. During the subsidence, the interior lithosphere remains welded to the exterior lithosphere. The differential subsidence causes upward flexure inside and downward flexure outside, forming the ridge, trench, and outer rise topography.

It should be noted that these models are not mutually exclusive. The main difference between the models is where the hot material is emplaced, above or below the preexisting lithosphere. In the tectonic scenario when subduction ceases and the corona reaches its final diameter, the interior lithosphere will be hot and thin, while the exterior lithosphere will be cold and thick. At this point the corona must go through a phase of differential thermal subsidence. Another possibility in the tectonic scenario is that the interior of the corona spreads radially but the preexisting lithosphere does not subduct. When the spreading ceases, the interior lithosphere will be hot relative to the exterior lithosphere and thus will undergo a final thermal subsidence phase. A calculation of the differential thermal subsidence is presented next to show that it can explain the small amplitude flexures observed at Heng-O but cannot produce the large trenches and outer rises at Eithinoha, Artemis, and Latona.

Differential Thermal Subsidence

The model incorporates two-dimensional cooling, thermal subsidence, and flexure of welded adjacent lithosphere of different ages [Sandwell and Schubert, 1982; Sandwell, 1984] (Figure 15). As in the previous section, it is assumed that the coronae have sufficiently large radii that their circularity is unimportant in the evolution of the flexural topography. In the initial state, it is assumed that 200-m.y.-old Venusian lithosphere outside of the corona abuts younger lithosphere of age 10 m.y. inside of the corona. The initial thermal profiles far from the contact zone are given by the classical error function solution of the one-dimensional cooling half-space model [Turcotte and Schubert, 1982] where the temperature at the surface of the lithosphere is T_0 and the deep mantle temperature is T_m (see Table 1 for values). The rate of heat diffusion is controlled by the thermal diffusivity κ . The temperature distribution in the vicinity of the contact zone is smoothed by allowing heat to diffuse across the zone for 10 m.y. The rheology of the lithosphere is considered to be perfectly elastic at depths less than the elastic isotherm T_e of 1023 K (750°C) and ductile or fluid at greater depths. The ductile material (Figure 15) can support the small buoyancy forces due to thermal contraction but cannot support the larger flexural stresses. Because of the sharp temperature contrast, there is a large change in elastic thickness across the contact zone. The initial elastic thickness of the interior lithosphere is 7 km, while the initial elastic thickness of the exterior lithosphere is 42 km. The initial state is assumed to be an unstressed configuration.

The relative sharpness of the initial thermal transition across the contact zone is essential for the subsequent development of a flexural moat and ridge topography. The model does not address the physics of how such a sharp thermal transition is established. The sketch in Figure 14 suggests that the initial state is the product of the reheating and thinning of the lithosphere above a mantle plume. However, the mathematical model of the development of flexural moat and ridge topography applies no matter how the "initial" plateaulike state is formed.

The interior lithosphere (Figure 16, $x > 0$) is allowed to cool with time while the exterior lithosphere does not cool with time

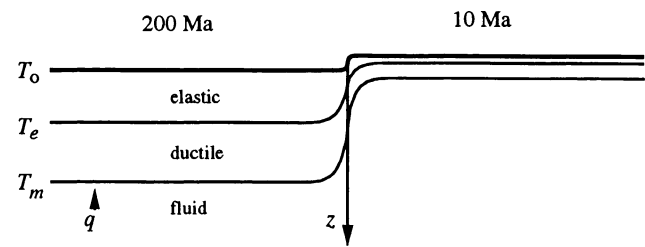


Fig. 15. Diagram showing the initial conditions of the differential thermal subsidence model. The base of the thermal boundary layer (i.e., lithosphere) is defined by the T_m isotherm, while the base of the elastic plate is defined by the T_e isotherm. The interior lithosphere (right side) is hot, thin, and elevated relative to the exterior lithosphere. The interior lithosphere cools and subsides with time, while the exterior lithosphere maintains its temperature profile by a constant background mantle heat flux q .

because its geotherm is maintained by a constant background mantle heat flux q . As the interior lithosphere cools and thickens with time, its average density increases. (The thermal expansivity α is given in Table 1.) Far from the contact zone, the lithosphere subsides isostatically at a rate proportional to the square root of time (Figure 16, dotted curves). After 200 m.y. of cooling, the interior has reached the same level as the exterior. Within about 150 km on either side of the contact zone, however, the lithosphere flexes to accommodate the differential thermal subsidence. The form of the flexure and the predicted surface stress depend on both the subsidence history and the lateral variations in elastic thickness. The flexure solution is obtained by summing flexures that have accumulated over small time increments. At each time step the differential equation is solved by an iteration method to account for the spatial variations in flexural rigidity.

The predictions of this simple thermal subsidence model compare favorably with topographic profiles across Heng-O. For example, outboard of the ridge (-400 km to 50 km, Figure 16) profile 501 matches the model topography curve corresponding to complete thermal subsidence (200 m.y.). Inboard of the ridge the model topography does not match the observations. It should be pointed out that the only adjustable parameters in the model are the initial ages of the interior and exterior lithospheres and the sharpness of the contact zone. These ages set the amplitude of the initial step offset as well as the elastic thicknesses of the interior and exterior lithospheres. In this case, the amplitude of the final ridge, trough, and outer rise flexure is about one half of the initial step amplitude.

None of the thermal subsidence profiles match the topography of Latona as shown in Figure 16. Removal of a linear topographic gradient would improve the fit on the exterior topography, but the model trench would be much too small (-400 km to -200 km, Figure 16). The model also does not fit any of the Artemis profiles because the amplitude of the model flexural topography is about a factor of 5 too small. One could increase the amplitude of the model topography by increasing the age contrast between the interior and exterior lithospheres. However, since thermal subsidence is proportional to the square root of age, the model age contrast must be increased to an absurd value of 5 b.y. which exceeds the age of the planet. These results suggest that differential thermal subsidence may be an important process for the majority of coronae that have relatively small amplitude flexures, but they cannot explain the larger flexures at Artemis and Latona.

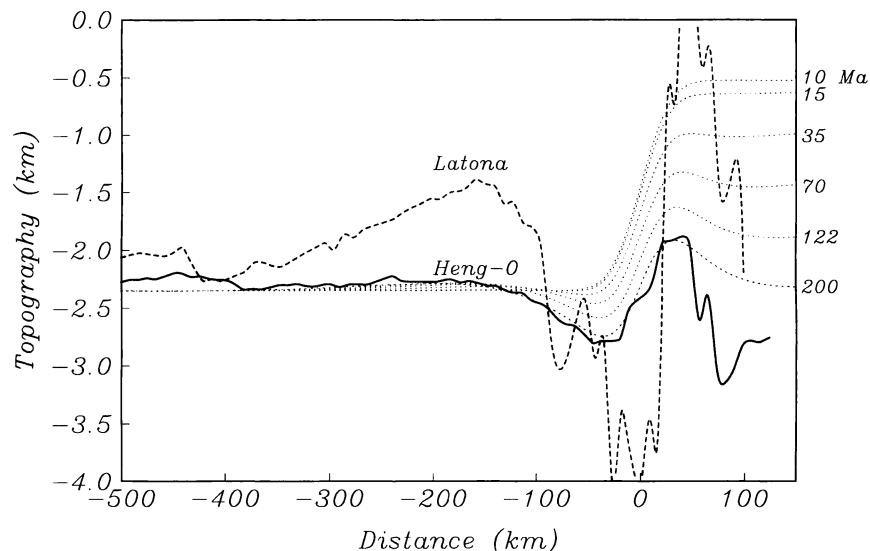


Fig. 16. Evolution of the topography for the differential thermal subsidence model (dotted curves). The thermal perturbation has decayed after 200 m.y. of cooling. The topography of Heng-O is well matched by the 200-m.y. model, while the topography of Latona cannot be fit by the model.

Subduction Model

The flexural trench and outer rise topography observed at Eithinoha, Artemis, and Latona is similar to flexural topography observed on the seaward side of subduction zones on Earth. For example, at Eithinoha the elastic plate is relatively thin (~ 15 km) and the bending moment at the trench axis is small (0.9×10^{16} N). This compares favorably with the thin plate (~ 12 km) and small moment (0.6×10^{16} N) observed at the Middle America Trench. In contrast, at Artemis the elastic plate is relatively thick (~ 37 km) and the bending moment is relatively large (25×10^{16} N). This compares favorably with an elastic thickness of 29 km and a maximum bending moment of 13×10^{16} N found at the Mariana Trench [Caldwell *et al.*, 1976]. Similarly, at Latona the elastic thickness and bending moment are 35 km and $\sim 6.0 \times 10^{16}$ N, respectively which compares favorably with the Aleutian Trench (28 km and 8.9×10^{16} N). On the Earth, the bending moment is primarily supplied by the negative buoyancy of the subducted lithosphere. The overriding plate is almost locally compensated so that it exerts almost no downward force on the subducting plate. Moreover, in many cases, the overriding plate is in a state of tension which results in back-arc spreading that is nearly parallel to the subduction zone [Barker and Hill, 1981]. As a final analogy, McKenzie *et al.* [this issue] have noticed that many of the arclike topographic structures in eastern Aphrodite Terra (including Latona and northern Artemis) have similar morphology and scale to subduction zones in the East Indies on Earth. In both cases, the subduction zones are curved with the high topography on the concave side.

On Earth, the negative buoyancy of the subducted lithosphere acts as a stress guide that draws the not yet subducted lithosphere into the trench. This effect (slab pull) is believed to be the major driving force of plate tectonics [Schubert, 1980]. An unusual feature of some coronae including Eithinoha, Artemis and Latona is that the trench wraps around the corona by more than 180° . Thus if the trench axis were to remain stationary, the entire lithosphere would have to compress and thicken as it moved into the trench. Because this seems physically implausible and there are no indications of circumferential compression outboard of the trench, we prefer the model where the trench axis rolls back and the corona increases in diameter.

SUMMARY

1. High-resolution altimetry collected by the Magellan spacecraft has revealed trench and outer rise topographic signatures around many major coronae [Stofan *et al.*, this issue]. In addition, Magellan SAR images show circumferential fractures in areas where the plates are curved downward. These observations suggest that the lithosphere around coronae is flexed downward either by the weight of the overriding coronal rim or by the negative buoyancy of subducted lithosphere.

2. We have selected four of the largest coronae (Eithinoha, Heng-O, Artemis, and Latona) which display these flexural characteristics and have modelled the trench and outer rise topography as a thin elastic plate subjected to a line load and bending moment beneath the corona rim. The elastic thicknesses determined by modelling numerous profiles at Eithinoha, Heng-O, Artemis, and Latona are 15, 40, 37, and 35 km, respectively. At Eithinoha, Artemis, and Latona where the plates appear to be yielding, the maximum bending moments and elastic thicknesses are similar to those found at the Middle America, Mariana, and Aleutian trenches on Earth, respectively.

3. Estimates of effective elastic thickness and plate curvature are used with a yield strength envelope model of the lithosphere to estimate lithospheric temperature gradients. At Heng-O, Artemis, and Latona, temperature gradients are less than 10 K/km which correspond to conductive heat losses of less than one half the expected average planetary value. There are many possible explanations for the low estimated heat flows. However, modelling of many more areas is needed to establish a planetary average.

4. We propose two scenarios for the creation of the ridge, trench and outer rise topography: differential thermal subsidence and lithospheric subduction. The topography of Heng-O is well matched by the differential thermal subsidence model. However at Artemis and Latona, the amplitudes of the trench and outer rise signatures are a factor of 5 too large to be explained by thermal subsidence alone. In these cases we favor the lithospheric subduction model wherein the lithosphere outboard of the corona perimeter subducts (rolls back) and the corona diameter increases.

Acknowledgments. We thank Peter Ford for providing an updated version of the altimeter profiles and many technicians at Jet Propulsion Laboratory for processing of the SAR images. Ellen Stofan, Duane Bindschadler, Buck Janes, and Stephen Squyres organized the coronae SAR data into a very usable format. Barry Parsons provided helpful suggestions on modelling the trench/outer rise flexure. Dan McKenzie contributed to many of the ideas related to the subduction zone hypothesis and provided feedback on many aspects of the research. The research was partially supported by the Magellan Project (JPL 958950 and JPL 958496).

REFERENCES

- Barker, P. F., and I. A. Hill, Back-arc extension in the Scotia Sea, *Philos. Trans. R. Soc. London Ser. A*, **300**, 249-262, 1981.
- Barsukov, V. L., et al., The geology and geomorphology of the Venus surface as revealed by the radar images obtained by Veneras 15 and 16, *J. Geophys. Res.*, **91**, 378-398, 1986.
- Basilevsky, A. T., A. A. Pronin, L. B. Ronca, V. P. Kryuchkov, A. L. Sukhanov, and M. S. Markov, Styles of tectonic deformation on Venus: Analysis of Veneras 15 and 16 data, *J. Geophys. Res.*, **91**, 399-411, 1986.
- Bindschadler, D. L., and E. M. Parmentier, Mantle flow tectonics and a ductile lower crust: Implications for the formation of large-scale features on Venus, *J. Geophys. Res.*, **95**, 21329-21344, 1990.
- Byerlee, J. D., Friction of rocks, *Pure Appl. Geophys.*, **116**, 615-626, 1978.
- Caldwell, J. G., W. F. Haxby, D. E. Karig, and D. L. Turcotte, On the applicability of a universal elastic trench profile, *Earth Planet. Sci. Lett.*, **31**, 239-246, 1976.
- Comer, R. P., S. C. Solomon, and J. W. Head, Mars: Thickness of the lithosphere from the tectonic response to volcanic loads, *Rev. Geophys.*, **23**, 61-92, 1985.
- De Bremaecker, J. C., Is the oceanic lithosphere elastic or viscous?, *J. Geophys. Res.*, **82**, 2001-2004, 1977.
- Ford, P. G., and G. H. Pettengill, Venus topography and kilometer-scale slopes, *J. Geophys. Res.*, this issue.
- Goetze, C., and B. Evans, Stress and temperature in the bending lithosphere as constrained by experimental rock mechanics, *Geophys. J. R. Astron. Soc.*, **59**, 463-478, 1979.
- Lawson, C. L., and R. J. Hanson, *Solving Least Squares Problems*, Prentice Hall, Englewood Cliffs, N.J., 1974.
- McAdoo, D. C., C. F. Martin and S. Poulouse, Seasat observations of flexure: Evidence for a strong lithosphere, *Tectonophysics*, **116**, 209-222, 1985.
- McKenzie, D., P. G. Ford, C. Johnson, B. Parsons, D. Sandwell, S. Saunders, and S. C. Solomon, Features of Venus generated by plate boundary processes, *J. Geophys. Res.*, this issue.
- McNutt, M. K., Lithospheric flexure and thermal anomalies, *J. Geophys. Res.*, **89**, 11,180-11,194, 1984.
- Melosh, H. J., Dynamic support of outer rise topography, *Geophys. Res. Lett.*, **5**, 321-324, 1978.
- Parsons, B., and P. Molnar, The origin of outer topographic rises associated with trenches, *Geophys. J. R. Astron. Soc.*, **45**, 707-712, 1976.
- Pettengill, G. H., P. G. Ford, W. T. K. Johnson, R. K. Raney, and L. A. Soderblom, Magellan: Radar performance and data products, *Science*, **252**, 260-265, 1991.
- Pronin, A. A., and E. R. Stofan, Coronae on Venus: Morphology and distribution, *Icarus*, **87**, 452-474, 1990.
- Sandwell, D. T., Thermomechanical evolution of oceanic fracture zones, *J. Geophys. Res.*, **89**, 11,401-11,413, 1984.
- Sandwell, D., and G. Schubert, Lithospheric flexure at fracture zones, *J. Geophys. Res.*, **87**, 4657-4667, 1982.
- Sandwell, D. T., and G. Schubert, Lithospheric flexure due to thermal subsidence of coronae (abstract), *Eos Trans. AGU*, **72(17)**, Spring Meeting Suppl., 174, 1991.
- Schubert, G., Self-driven motions of plates and descending slabs, in *Plate Tectonics and Mechanisms of Continental Drift*, edited by P. A. Davies and S. K. Runcorn, pp. 151-158, Academic, San Diego, Calif., 1980.
- Solomon, S. C., and J. W. Head, Lithospheric flexure beneath the Freyja Montes foredeep, Venus: Constraints on lithospheric thermal gradient and heat flow, *Geophys. Res. Lett.*, **17**, 1393-1396, 1990.
- Solomon, S. C., J. W. Head, W. M. Kaula, D. McKenzie, B. Parsons, R. J. Phillips, G. Schubert, and M. Talwani, Venus tectonics: Initial analysis from Magellan, *Science*, **252**, 297-312, 1991.
- Squyres, S. W., D. M. Jones, G. Baer, D. L. Bindschadler, G. Schubert, V. L. Sharpton, and E. R. Stofan, The morphology and evolution of coronae on Venus, *in press J. Geophys. Res.*, this issue.
- Stofan, E. R., and J. W. Head, Coronae of Mnemosyne Regio, Venus: Morphology and origin, *Icarus*, **83**, 216-243, 1990.
- Stofan, E. R., D. L. Bindschadler, J. W. Head, and E. M. Parmentier, Corona structures on Venus: Models of origin, *J. Geophys. Res.*, **96**, 20,933-20,946, 1991.
- Stofan, E. R., V. L. Sharpton, G. Schubert, G. Baer, D. L. Bindschadler, B. M. Janes and S. W. Squyres, Global distribution and characteristics of coronae and related structures on Venus: Implications for origin and relation to mantle processes, *J. Geophys. Res.*, this issue.
- Turcotte, D. L., and G. Schubert, *Geodynamics*, John Wiley, New York, 1982.
- Walcott, R. I., Flexure of the lithosphere at Hawaii, *Tectonophysics*, **9**, 435-446, 1970.

D. T. Sandwell, Geological Research Division, Scripps Institution of Oceanography, San Diego, La Jolla, CA 92093-0220.

G. Schubert, Department of Earth Space Sciences, IGPP, University of California, Los Angeles, CA 90024.

(Received October 15, 1991;
revised June 4, 1992;
accepted June 4, 1992.)